



Structural phase analysis, optical and magnetic properties of nano Mn-doped LiFe_5O_8

Zein K. Heiba² · Mohamed Bakr Mohamed^{1,2}

Received: 14 September 2018 / Accepted: 8 November 2018 / Published online: 14 November 2018
© Springer-Verlag GmbH Germany, part of Springer Nature 2018

Abstract

Nano Mn-doped LiFe_5O_8 was synthesized by citrate procedure. Structural and microstructure investigations have been performed applying X-ray diffraction (XRD), neutron powder diffraction (NPD), Fourier transform infrared spectroscopy (FTIR) and transmission electron microscope (TEM). Field-cooled (FC) and zero field-cooled (ZFC) dc magnetization were measured using a SQUID magnetometer. Law of Approach to saturation model was applied on hysteresis loops measured by vibrating sample magnetometer (VSM) at room temperature to obtain the saturation magnetization and magneto anisotropy constant for all samples. Rietveld analysis of XRD and NPD revealed that LiFe_5O_8 has ordered cubic structure with space group $P4_332$. On the other hand XRD and FTIR analyses revealed that Mn-doped LiFe_5O_8 system has biphasic structures; cubic with ordered phase ($P4_332$) and disordered one ($Fd\bar{3}m$). TEM image shown that the sample has an average particle size ~ 14 nm. Applying a propagation vector $\mathbf{k}=(0\ 0\ 0)$, all magnetic peaks of NPD data at 4 K are indexed with total magnetic moment = 1.8 μB . The coercivity and saturation magnetization reduced generally with raising the amount of Mn doping. Photoluminescence spectra of all samples exhibited two UV and one green sub-emissions.

1 Introduction

Lithium ferrites, especially LiFe_5O_8 or $\text{Li}_{0.5}\text{Fe}_{2.5}\text{O}_4$, are important candidates of ferrite family which have the privileges of low cost and preserving the environment [1]. They have been extensively investigated for many applications in various technological areas, for example microwave devices [2], opto-isolators [3], and electrode materials for lithium ion batteries [4]. LiFe_5O_8 possess high Curie temperature (~ 900 K) [5] and high saturation magnetization (~ 60 emu/gm) [6]. LiFe_5O_8 has two spinel structures [7]: order structure (α -phase) which occurred at low temperature and disorder structures (β -phase) formed above 735–755 °C. The ordered structure has a cubic primitive tetragonal unit cell ($P4_332$) with Li^+ : Fe^{3+} cation ordering of ratio 1:3, where the Fe^{3+} ions are sited at 12d octahedral and 8c tetrahedral positions, while Li^+ ions are occupied only the 4b octahedral sites. The disordered phase has FCC unit cell with

spinel structure ($Fd\bar{3}m$), where 8a tetrahedral site is occupied only by Fe^{3+} whereas the 16d octahedral site is shared by Fe^{3+} and Li^+ ions randomly. For bulk $\text{Li}_{0.5}\text{Fe}_{2.5}\text{O}_4$, the order to disorder phase transition occurs in the temperature range 1008–1028 K [8]. Generally, the properties of ferrite can be tuned either by doping it with a suitable element, changing the annealing temperature or choosing different preparation methods [9]. Jovic et al. [10] explored the effect of annealing temperature on the crystal structure of nano $\text{Li}_{0.5}\text{Fe}_{2.5}\text{O}_4$; they found that up to 673 K, Li^+ and Fe^{3+} ions have a partial ordering between the 4b and 12d octahedral sites of the primitive spinel lattice ($P4_332$). Upon annealing at 973 K, the cation distribution changed to a completely ordered structure. Applying a microwave-induced combustion procedure at 650 °C, Fu et al. [11] prepared a single disorder phase from $\text{Li}_{0.5}\text{Fe}_{2.5-x}\text{Mn}_x\text{O}_4$ ($0 \leq x \leq 1.0$); but below 650 °C and above 850 °C, an additional phase ($\alpha\text{Fe}_2\text{O}_3$) was formed. Hankare et al. [12] prepared $\text{Li}_{0.5}\text{Fe}_{2.5-x}\text{Mn}_x\text{O}_4$ ($0 \leq x \leq 2.5$) utilizing an auto combustion sol-gel procedure at 700 °C, they found that up to $x = 1.5$ a cubic disordered structure is formed, and above $x = 1.5$, the samples exhibited a tetragonal ordered phase. Widatallah et al. [13] showed using both Mössbauer and X-ray diffraction techniques that the nano $\text{Li}_{0.5}\text{Fe}_{2.5}\text{O}_4$ doped with Mn^{4+} has an inverse spinel structure (disordered, $Fd\bar{3}m$) with superparamagnetic nature.

✉ Mohamed Bakr Mohamed
mbm1977@yahoo.com

¹ Physics Department, Faculty of Science, Taibah University, Al-Madinah Al-Munawara, Saudi Arabia

² Department of Physics, Faculty of Science, Ain shams University, Cairo 11566, Egypt

Kounsalye et al. [14] prepared Ti^{4+} -doped $\text{Li}_{0.5}\text{Fe}_{2.5}\text{O}_4$ by sol–gel auto combustion technique at 650 °C and they found the phase transformation from $\text{P4}_3\text{32}$ to $\text{Fd}\bar{3}\text{m}$ structure occurred upon doping. Sharma et al. [15] prepared $\text{Li}_{0.5}\text{Co}_x\text{Fe}_{2.5-x}\text{O}_4$ by citrate precursor method at 900 °C and they claimed that the system has an order structure for undoped and Co-doped samples, but closely look in their XRD and IR data the undoped sample has order structure but the order/disorder structure appeared in all doped samples. In this work undoped and doped $\text{Li}_{0.5}\text{Fe}_{2.5}\text{O}_4$ with Mn were prepared using a citrate procedure at low temperature 400 °C. The magnetic structure of $\text{Li}_{0.5}\text{Fe}_{2.5}\text{O}_4$ is studied in detail using neutron powder diffraction technique and Fullprof software was applied. The structure phase transition as Mn-doped $\text{Li}_{0.5}\text{Fe}_{2.5}\text{O}_4$, phases percentage, crystallite size and microstrain are investigated by X-ray diffraction analysis using MAUD software, Fourier transform infrared spectroscopy, and transmission electron microscope. The magnetic and photoluminescence (PL) properties of undoped and doped $\text{Li}_{0.5}\text{Fe}_{2.5}\text{O}_4$ with Mn are also studied in details using SQUID, vibrating sample magnetometer and luminescence spectrophotometer techniques.

2 Experimental

Nano $\text{Li}_{0.5}\text{Fe}_{2.5-x}\text{Mn}_x\text{O}_4$ ($x=0, 0.25, 0.5, 0.75, 1$) samples were synthesized by stirring a required amount of iron, manganese, lithium nitrates and citric acid in a minimum amount of deionized water at 70 °C for 4 h and then the formed gel was heated at 400 °C (1 h). X-ray diffraction data for all samples were collected by Philips X-ray diffractometer (X'pert MPD, Cu- $\text{K}\alpha$). The crystal structure and microstructure of the undoped and doped samples were refined using MAUD program which was based on Rietveld analysis [16]. Fullprof program package [17], also based on Rietveld profile method was applied to find the crystal and magnetic structures [18] of $\text{Li}_{0.5}\text{Fe}_{2.5}\text{O}_4$ using neutron powder diffraction data (SPODI at FRMII, Technical university, Munich, Germany); at 3 and 300 K with $\lambda = 1.5487$ Å. FTIR spectra were recorded (Bruker Tensor 27 FTIR Spectrometer) with a frequency range of 400–800 cm^{-1} . Photoluminescence (PL) measurement was carried out by luminescence spectrophotometer (RF-1501 SHIMADZU, Ltd) with a resolution of 10 nm. The temperature depends of magnetization in zero field-cooled (ZFC) and field-cooled (FC) modes and also M-H hysteresis curve at 3 K under applied magnetic fields ranging up to 60 kOe were performed for $\text{Li}_{0.5}\text{Fe}_{2.5}\text{O}_4$ using SQUID magnetometer. Moreover, M-H hysteresis curves for $\text{Li}_{0.5}\text{Fe}_{2.5-x}\text{Mn}_x\text{O}_4$ were measured at room temperature with magnetic field up to 20 kOe, using the LDJ vibrating sample magnetometer (VSM) model 9600. Transmission electron microscope (TEM, JEOL JEM-100CX, 100 kV) was used to

examine the particle shape and confirm the nano-size scale of the samples.

3 Results and discussion

3.1 Structure and microstructure analysis

Figure 1 reveals the X-ray diffraction data recorded for $\text{Li}_{0.5}\text{Fe}_{2.5-x}\text{Mn}_x\text{O}_4$ with $x=0.0, 0.25, 0.5, 0.75$ and 1.0. Phase identification was performed using the search-match program X'Pert HighScore Plus. The undoped sample $\text{Li}_{0.5}\text{Fe}_{2.5}\text{O}_4$ is found to be the ordered spinel phase ($\text{P4}_3\text{32}$), Fig. 2a. The microstructure analysis of this sample is performed in detail using neutron powder diffraction at 3 and 300 K. For Mn-doped samples, one can notice that the reflections (210), (211) and (310), characterizing the primitive $\text{P4}_3\text{32}$ phase, fade out upon Mn doping indicating the $\text{P4}_3\text{32} \rightarrow \text{Fd}\bar{3}\text{m}$ phase transition. Careful phase analysis of XRD data indicated the existence of mixed phases; disorder spinel $\text{Fd}\bar{3}\text{m}$ as a major phase (> 92%) and ordered spinel $\text{P4}_3\text{32}$ as a minor one (< 8%), Fig. 2b. The presence of the minor disordered phase may be attributed to the low temperature of preparation (400 °C). Results of Rietveld analysis for Mn-doped samples (disorder phase $\text{Fd}\bar{3}\text{m}$) are gathered in Table 1. The lattice parameter (a) remains almost constant (within standard deviation) unaffected by Mn substitution which can be attributed to the close values radii of Mn^{3+} (0.645 Å) and Fe^{3+} (0.64 Å) ions. Also, the z -coordinate for oxygen atom remains almost constant within standard deviation. Nano size is confirmed for all samples, the crystallite size ranges between 5 and 12 nm. From Table 1, upon raising the Mn amount, the part of Li ions residing at tetrahedral sites increased. Furthermore, Mn^{3+} preferred replacing Fe^{3+} at the octahedral sites pushing Li ions to tetrahedrons. However, it is well known that the cation distribution and ordering depends on preparation conditions [19–21]. The Fe^{3+} occupancy decreased in both tetrahedron and octahedron sites but with different rates; a result that has a direct impact on the magnetic properties. Figure 2c shows the TEM image for $\text{Li}_{0.5}\text{Mn}_{0.25}\text{Fe}_{2.25}\text{O}_4$, where the average particles size ≈ 14 nm in a reasonable agreement with the crystallite size revealed from XRD analysis. TEM figure also revealed humongous and isovolumetric morphology of prepared particles with some agglomeration occurring due to both very small size and magnetization.

The neutron diffraction data recorded at 3 and 300 K for $\text{Li}_{0.5}\text{Fe}_{2.5}\text{O}_4$ sample are depicted in Fig. 3. Only the crystal structure reflections are obtained with no extra magnetic reflections indicating that the chemical and magnetic cells are the same. Neutron diffraction data were analyzed based on Rietveld refinement using Fullprof software at 4 and 300 K, to determine first the occupancies of different ions at

Fig. 1 XRD diffraction for nano Li_{0.5}Fe_{2.5-x}Mn_xO₄

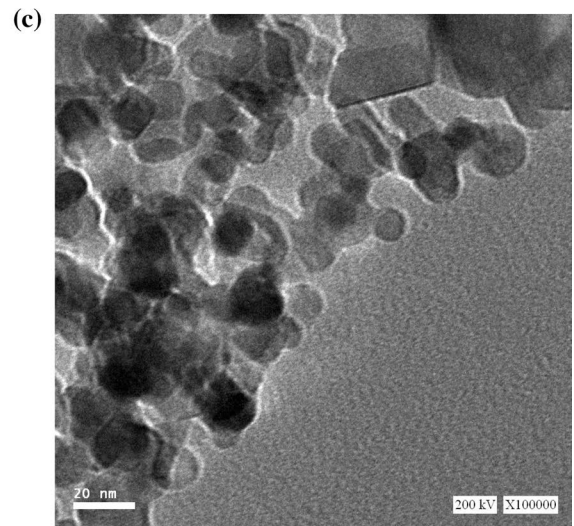
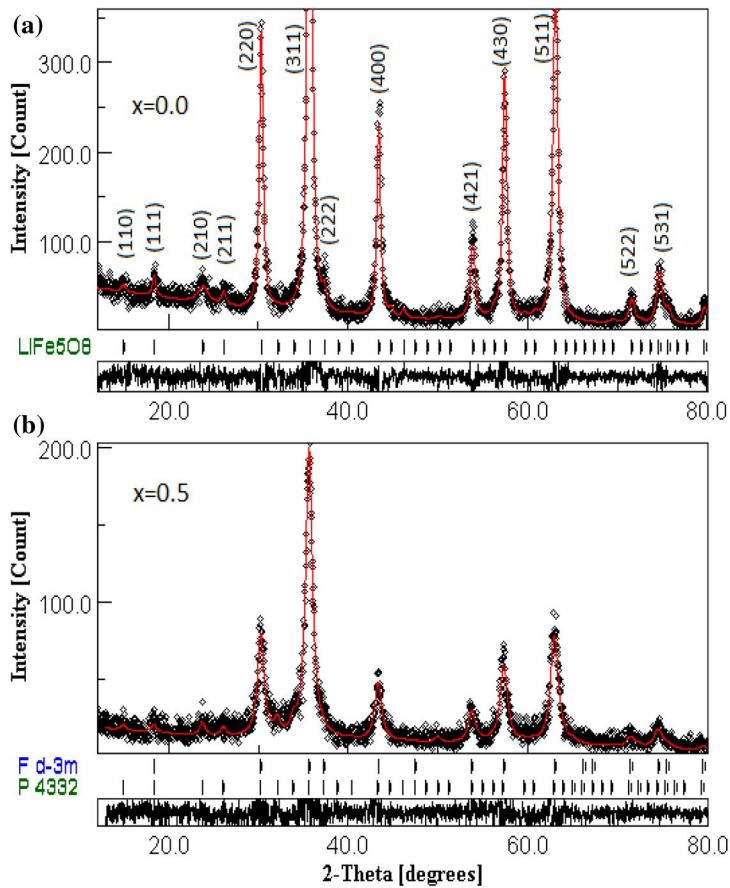
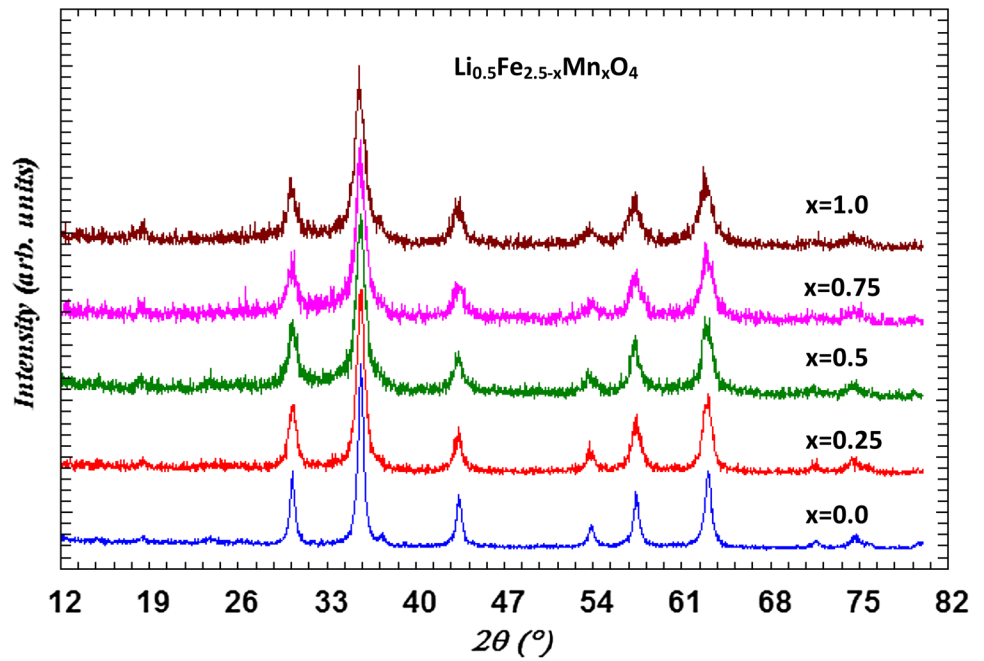


Fig. 2 a, b Rietveld refinement for Li_{0.5}Fe_{2.5}O₄ and Li_{0.5}Fe₂Mn_{0.5}O₄ and c TEM image for Li_{0.5}Mn_{0.25}Fe_{2.25}O₄

Table 1 Lattice parameter (a), oxygen position (u), crystallite size (CS), micro-strain (MS), occupancies of different cations in different sites and phase percentage of disorder phase with space group Fd3m for $\text{Li}_{0.5}\text{Fe}_{2.5-x}\text{Mn}_x\text{O}_4$ samples using X-ray diffraction data

x	0.25	0.5	0.75	1.0
a	8.3466 (71)	8.3457 (58)	8.3474 (27)	8.3506 (96)
u	0.2525 (12)	0.2522 (14)	0.2508 (18)	0.2547 (17)
Fd3m %	97.1	92.5	95.9	96.7
Occupancy factor				
A-site	Li 0.004 (35)	0.015 (38)	0.045 (52)	0.069 (49)
8a	Fe 0.996 (35)	0.985 (38)	0.955 (52)	0.931 (49)
B-site	Li 0.249 (35)	0.243 (38)	0.228 (52)	0.215 (49)
16d	Fe 0.627 (35)	0.507 (38)	0.397 (52)	0.285 (49)
	Mn 0.125 (35)	0.25 (38)	0.375 (52)	0.500 (49)
CS nm	12.3	11.3	10.4	5.5
$\text{MS} \times 10^{-6}$	8.3	7.9	2.8	4.8

different sites and second, the magnetic structure and hence the magnetic moment of different iron ions in different sites for $\text{Li}_{0.5}\text{Fe}_{2.5}\text{O}_4$ nanoparticle. Examining Fig. 3, one notices

the appearance of some reflections at low angles, indicating the existence of ordered tetragonal phase, $\text{P4}_3\text{32}$. During Rietveld refinements, attempts to treat pure $\text{Li}_{0.5}\text{Fe}_{2.5}\text{O}_4$ as biphasic, ordered and disordered, could not succeed. Also, comparing neutron powder diffraction patterns at 4 and 300 K, Fig. 3a, the intensity of some reflections of 4 K are increased with respect to pattern at 300 K. Due to similar magnetic and nuclear unit cells, all magnetic reflections are indexed with a propagation vector $\mathbf{k}=(0\ 0\ 0)$. The neutron diffraction patterns were investigated using Rietveld refinement assigning the space group $\text{P4}_3\text{32}$ and P-1 for nuclear and magnetic structures, respectively (Fig. 3b). The positions of magnetic ions in magnetic unit cell were generated using the BASIREPS [22], associated in Fullprof software where the iron ions have 24 position for space group $\text{P4}_3\text{32}$ compared to 6 position as in case of $\text{Fd}\bar{3}\text{m}$. The refined values of lattice parameter, ions occupancies for $\text{Li}_{0.5}\text{Fe}_{2.5}\text{O}_4$ at 300 K are listed in Table 2. The occupancies of iron, lithium and oxygen ions at different sites show that Li ions occupied B-site while Fe ions occupied both A and B-sites. Utilizing the obtained cation distribution and considering that Fe^{3+} is the only magnetic ion with spin moment ($5\ \mu_B$), the

Fig. 3 a Neutron diffraction of $\text{Li}_{0.5}\text{Fe}_{2.5}\text{O}_4$ at 4 and 300 K, b Rietveld refinement fitting of neutron diffraction data using Fullprof software, where the magnetic scattering from anti-ferromagnetically aligned Fe atoms on the A- and B-sites are included

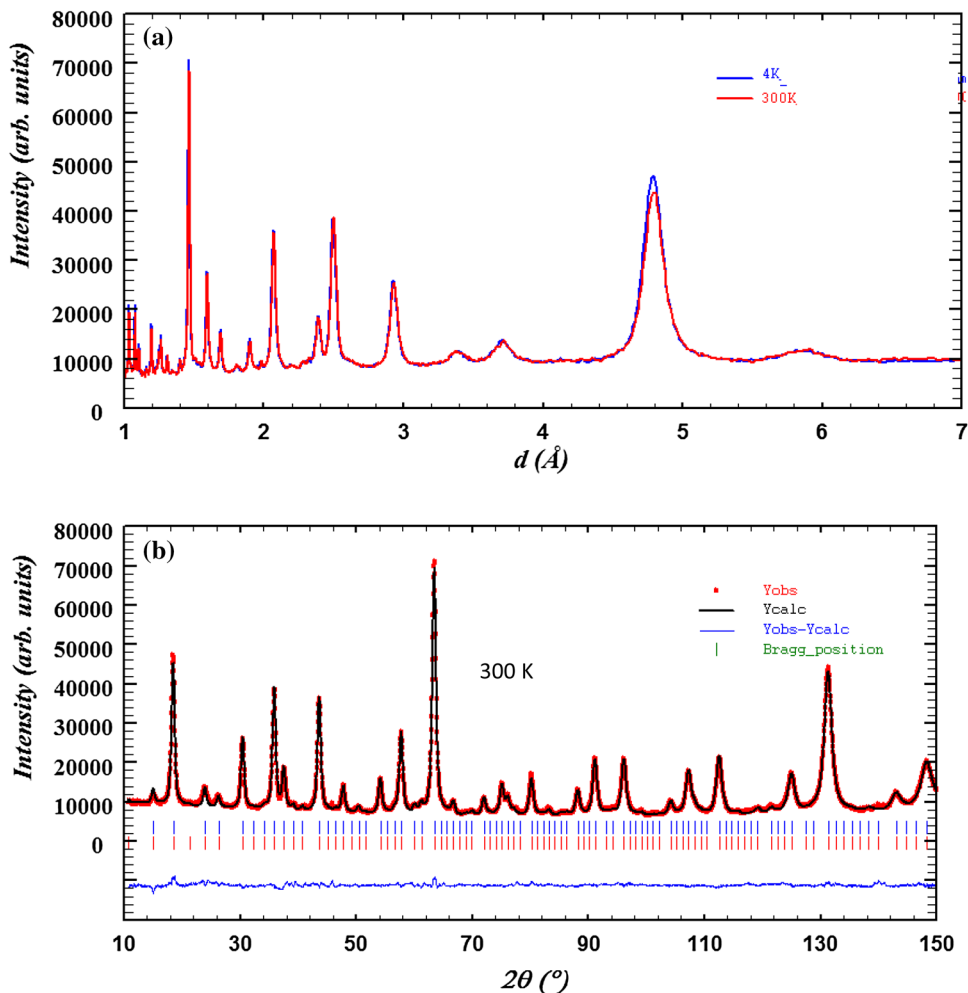


Table 2 Lattice parameter (*a*), occupancies of different cations in different sites and magnetic moment at each site with different error values for Li_{0.5}Fe_{2.5}O₄ sample using neutron powder diffraction data

	Site	<i>x</i>	<i>y</i>	<i>z</i>	occ.
Tetrahedral sites					
Fe	8c	0.00010	0.00010	0.00010	0.3333
Octahedral sites					
Li	4b	0.62500	0.62500	0.62500	0.12 (8)
Fe	4b	0.62500	0.62500	0.62500	0.03 (8)
Li	12d	0.12500	0.36898	-0.11898	0.02 (5)
Fe	12d	0.12500	0.36898	-0.11898	0.4 (7)
O	8c	0.38270	0.38270	0.38270	0.3333
O	24e	0.11987	0.12579	0.38411	1.00
Lattice parameter (<i>a</i>)		8.3224(8) Å			
<i>M_A</i> (ND at 4 K)		2.37 μ _B			
<i>M_B</i> (ND at 4 K)		4.2 μ _B			
<i>M_T</i> (ND at 4 K)		1.8 μ _B			
<i>R</i> values					
<i>R_p</i>		6.22			
<i>wR_p</i>		6.03			
<i>R_M</i>		6.132			
<i>R_B</i>		3.03			

sub-lattice magnetic moments and total magnetic moment ($M_T = M_B - M_A$) are calculated, Table 2. The total magnetic moment obtained from neutron analysis at 4 K is 1.8 μ_B. The experimental saturation magnetization value (2.2 μ_B), obtained from *M* vs. *H* graph at 3 K, Fig. 5b, which included comparative aim. The deviation between the magnetic moments estimated from the magnetic measurements and those calculated from the obtained cation occupation assuming totally collinear arrangement in each sub-lattice may be attribute to existence of non-collinear spin interactions, similar result was obtained previously in Li_{*x*}Mn_{3-*x*}Fe_{*y*}O₄ spinels system [23].

Infrared spectroscopy can be used to check whether the doped Mn system has space group Fd $\bar{3}$ m or/and P4₃32. Based on group theory and unit cell approximation: cubic spinel whether normal or inverse with the space group Fd $\bar{3}$ m has four infrared-active vibrations while order cubic with the space group P4₃21 has a great number of allowed modes (21 infrared-active bands) [24, 25]. Four parameters may change simultaneously as the material substituted with different ions and hence affect the infrared spectrum: mass of cation, the cation–oxygen bond strength, the cation–oxygen bond length, and the unit cell dimensions. Most of the transition metal spinel-type oxides display three infrared-active bands, manifested in the regions of spectra as shown in Fig. 4 for Li_{0.5}Fe_{2.5}O₄: the first primary band ν_1 at 588 cm⁻¹ is assigned to the vibrations of Fe–O (Fe³⁺) bond in the tetrahedral sites. The second primary band ν_2 at 420 cm⁻¹

is attributed to the vibrations of Fe–O (Fe³⁺) bond in the octahedral sites. The shoulders appeared at around 553, 681 and 709 cm⁻¹ is referred to the existence of the Fe²⁺ ions in the sample, which initiates Jahn–Teller distortion leading to a local deformation in the crystal field potential and therefore splitting of the absorption bands [26]. The third band ν^3 at \approx 553 cm⁻¹ can be attributed to Li–O vibrations [27]. Moreover, as the Mn concentration increased in the samples, the sub-bands begin to fade and shift to other frequencies. Indeed, the disappearance (or weakening) of the vibrational bands with $\nu > 650$ cm⁻¹ is a good indicator that the ordered phase (P4₃21) is not present or is a minor one [28]; the same result obtained earlier with Rietveld analysis.

3.2 Magnetic properties of Li_{0.5}Fe_{2.5-*x*}Mn_{*x*}O₄ nanoparticle

Figure 5a shows ZFC/FC modes of the magnetization-temperature dependence applying a low magnetic field (100 Oe) for Li_{0.5}Fe_{2.5}O₄. ZFC and FC curves exhibited a splitting due to the competition between the energy required for magnetic moments reorientation and the energy barrier related with the crystalline anisotropy [29]. As the temperature increased, ZFC magnetization increased while FC magnetization decreased. ZFC curve did not show any maximum indicating that the blocking temperature (*T_b*) is higher than 350 K. In ZFC mode, at low temperature and without applying any external magnetic field, the nanoparticles oriented randomly along easy axis and hence a low value of magnetization. As the temperature increased, the magnetic anisotropy within the smaller particles is overcome by the thermal energy, and the alignment of magnetization direction of these activated nanoparticles with the field direction leads to increase in the magnetization value. When the nanoparticles are cooled in the presence of magnetic field (FC mode), regardless of easy axis of magnetization, the net magnetic moments within the individual nanoparticles aligned along the field direction. Thus, pre-oriented nanoparticles in the field direction were frozen at low temperature leads to highest magnetization at the lowest cooled temperature. By increasing the temperature, the thermal energy randomizes the magnetization directions by lowering magnetic anisotropy and thus decreases the magnetization value continuously leading to paramagnetism beyond Curie temperature (*T_C*). *M*–*H* curves at room temperature are revealed in Fig. 6a for Li_{0.5}Fe_{2.5-*x*}Mn_{*x*}O₄ (0 ≤ *x* ≤ 1) samples. To obtain the saturation magnetization (*M_s*) and magnetocrystalline anisotropy field (*K₁*) of the samples, room temperature hysteresis loop was fitted using Law of Approach to saturation [30]:

$$M = M_s \left(1 - \frac{A}{H} - \frac{B}{H^2} \right) + \kappa H$$

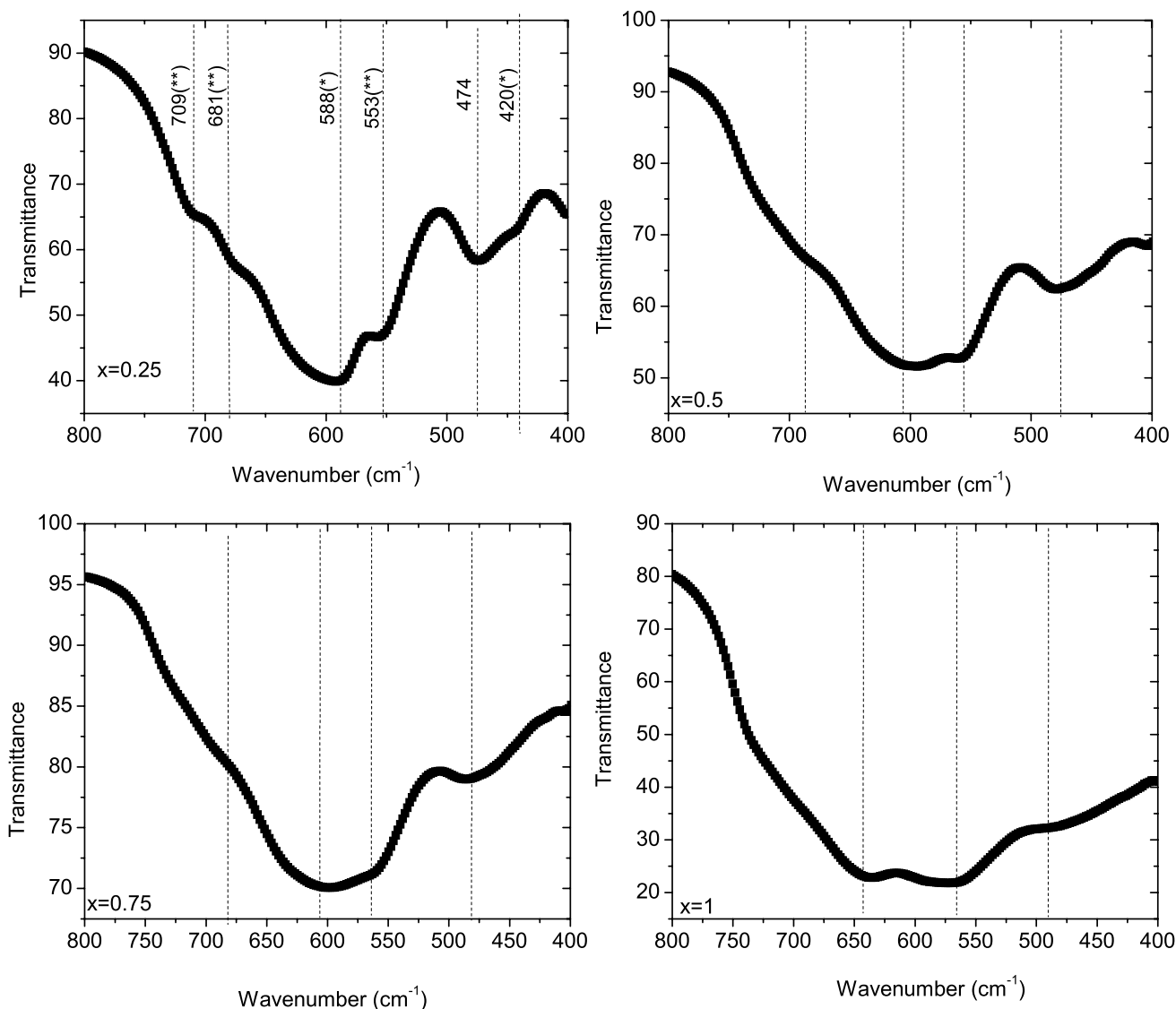


Fig. 4 FTIR for nano $\text{Li}_{0.5}\text{Fe}_{2.5-x}\text{Mn}_x\text{O}_4$ ($x=0.25, 0.5, 0.75, 1$)

where A and B are the constants associated to inhomogeneities and magnetocrystalline anisotropy of samples, respectively. The last term (κH) represented the high field differential susceptibility related to the spontaneous magnetization of the domains, and is active in the high temperature. Due to the small value of A/H and since our magnetic measurement was performed in room temperature, the last equation can be rewritten as

$$M = M_s \left(1 - \frac{B}{H^2} \right)$$

The values of M_s and B can be obtained from the intercept and slope of the linear relation between M and $1/H^2$, Fig. 6. The anisotropy field can be calculated from the relation for cubic anisotropy of random polycrystalline materials [31];

$$K_1 = \frac{M_s}{2} \sqrt{15B}$$

The saturation magnetization (M_s), the remanence magnetization (M_r), the coercivity (H_C) and magneto anisotropy constant (K_1) are listed in Table 3. From this table, one finds that the saturation magnetization of $\text{Li}_{0.5}\text{Fe}_{2.5}\text{O}_4$ (34.80 emu/g) is smaller than the value obtained for a sample prepared by microwave-induced combustion at 650 °C ($M_s = 71$ emu/g) [11] and also less than 63 emu/g in case of the same composition formed by sol-gel auto combustion procedure at 500 °C [32]; which may be due to the high annealing temperature used in preparation of the previous works [11, 32] and hence better crystallinity. As the amount of Mn increased up to =0.5, M_s decreased then it increased

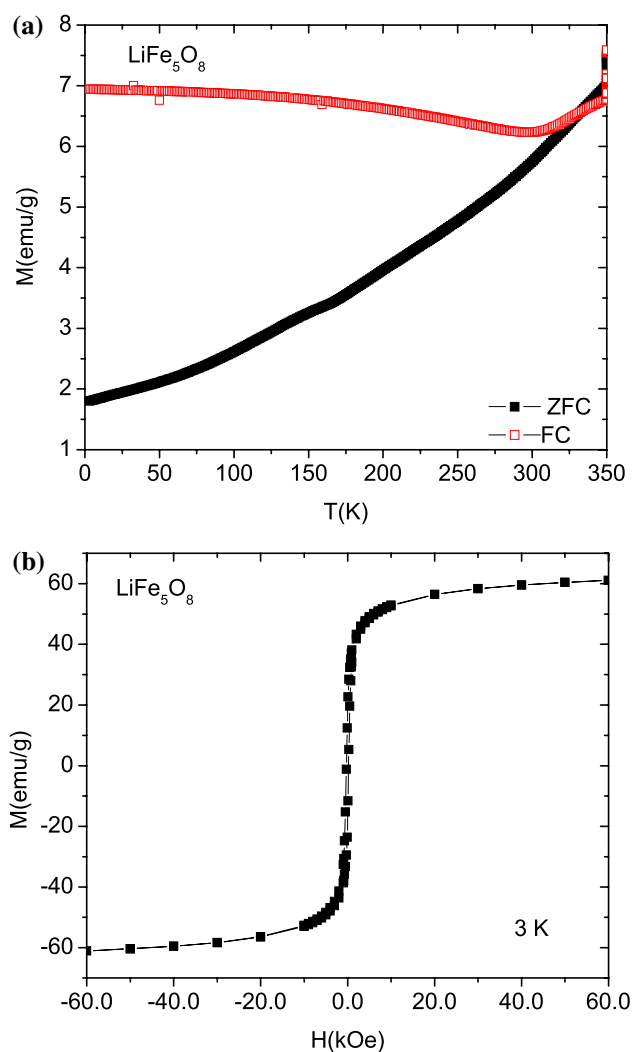


Fig. 5 **a** Field-cooled (FC)-Zero field-cooled (ZFC) magnetization as a function of temperature under an applied field of 100 Oe and **b** plot of magnetization as a function of the applied field at 3 K for Li_{0.5}Fe_{2.5}O₄ nanoparticles

at $x=0.75$ and finally reduced with further amount of Mn, Fig. 7a.

It is known that Mn³⁺ ions occupied the B-site but Mn²⁺ can occupy A- and B-sites [33], on the other hand, Fe³⁺ ions occupy both A- and B-sites while Fe²⁺ ions occupy only the B-sites [34]. The experimentally deduced value for the magnetic moment per formula unit n_{exp} was estimated from the measured M_S value applying the empirical relation [33]

$$n_{\text{exp}} = Mw \times M_S / 5585$$

To explain the behavior of M_S , the ordering of different cations between A- and B-site can be described by a collinear Néel two-sub-lattice model [33]:

$$n_{\text{cal}} = M_B - M_A$$

where M_A and M_B are magnetization of the tetrahedron and octahedron sub-lattices, respectively, which can be estimated using the cation magnetic moments in terms of the Bohr magneton (μ_B); Fe³⁺, Fe²⁺, Mn³⁺ Mn²⁺ and Li⁺ have 5, 4, 4, 5 and 0 μ_B , respectively. The comparison between n_{exp} and n_{cal} (based on the cation occupancies got from XRD refinement, Table 1) is shown in Fig. 7b, where both n_{exp} and n_{cal} exhibited a similar trend. Residing Mn³⁺ ions at B-site in the place of Fe³⁺ ions obviously decreases the saturation magnetization of sub-lattice B. Due to the possibility that some manganese ions are converted into Mn²⁺ in the B-site, the magnetization increased in some concentration. On the other hand, the remnant magnetization is reduced by doping the samples with Mn ions as compared with undoped sample which may be caused by the lesser exchange interactions [35]. The low values of M_r/M_S ratio indicated a significant part of superparamagnetic particles. On the other hand, H_c decreased irregularly with increased amount of Mn doping, a similar result was obtained in nano-crystalline Co_{1-x}Mn_xFe_{2-2x}Mn_{2x}O₄ [36]. In a single domain region the coercivity and crystallite size are related as [37]

$$H_c = g - \frac{h}{D^2}$$

where, g and h are constants.

So, decreasing the crystallite size led to decrease the coercivity due to the thermal effect. The crystallite sizes of the Mn-substituted samples are within limit of single domain and, thus the coercivity is reduced with decreasing of crystallite size [38]. Also as seen from Table 1 the magneto anisotropy constant (K_1) decreased as the amount of Mn increased in Li-ferrite sample. A similar effect was observed in Co_{1-x}Mn_xFe₂O₄ and CoMn_xFe_{2-x}O₄ systems [36, 39], and this decreasing can be explained by reduction of occupancy of Co ions at the B-sites as Mn amount increased in B-site or/and surface strain effect. As seen from Table 1, the crystallite size reduced with increased amount of Mn and this reduction in size led to large surface to volume atoms. Therefore, surface strain become dominate at the surface of the samples, i.e., crystal lattice are not in well-defined order which may perturb the crystal symmetry at the surface and, hence affects the magnetocrystalline anisotropy [39].

3.3 Optical properties of Li_{0.5}Fe_{2.5-x}Mn_xO₄ nanoparticles

Figure 8 shows the photoluminescence (PL) emission of LiFe₅O₈ doped with Mn under excitation wavelength 220 nm in emission range 230–700 nm. It is clear from the figure that the PL emission band is asymmetrical and broadened with multiple peaks indicating the contribution of various luminescence centers in the radiative procedure. The PL intensity decreased as the amount of Mn entering Lithium

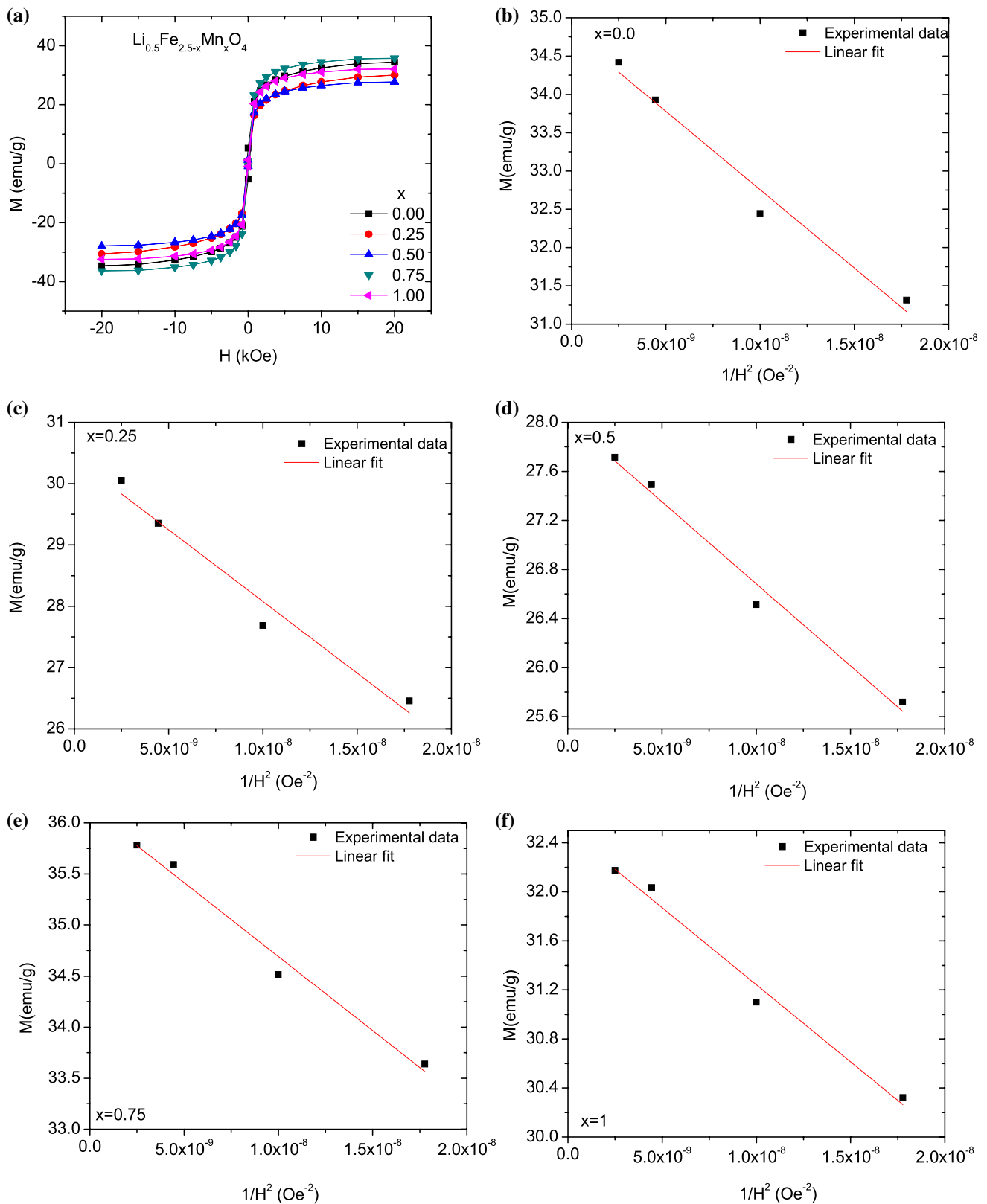
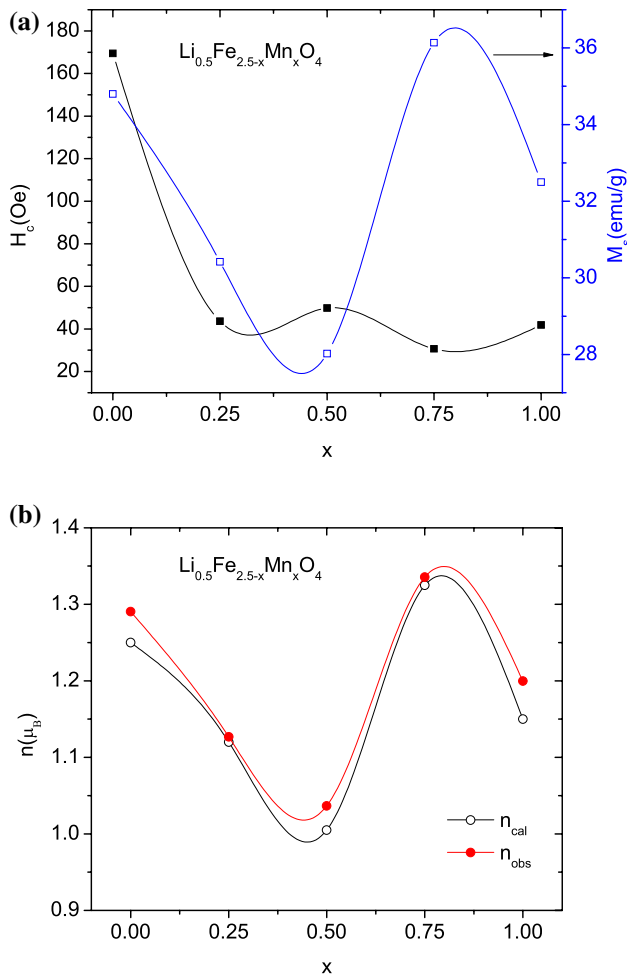


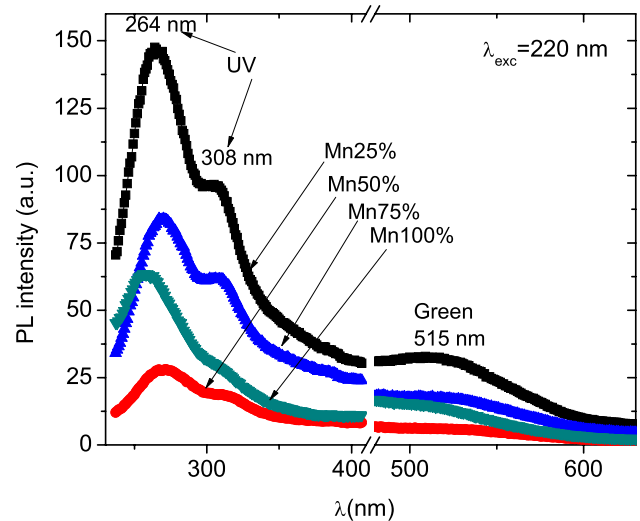
Fig. 6 a Plot of magnetization as a function of the applied field at room temperature and **b–f** magnetization versus $1/H^2$ plots with fitting using Law of Approach to saturation model for $\text{Li}_{0.5}\text{Fe}_{2.5-x}\text{Mn}_x\text{O}_4$ nanoparticles

Table 3 Magnetic parameters for Li_{0.5}Fe_{2.5-x}Mn_xO₄ samples at room temperature

<i>x</i>	<i>H_c</i> (Oe)	<i>M_S</i> (emu/g)	<i>M_r</i> (emu/g)	<i>M_r/M_s</i>	<i>K₁</i> (10 ⁵ erg/cm ³)
0.0	169.49	34.802	5.2691	0.15257	1.634
0.25	43.555	30.419	0.91238	0.0301	1.634
0.5	49.82	28.021	1.1031	0.03968	1.186
0.75	30.629	36.139	0.89575	0.02482	1.401
1.0	41.847	32.499	1.0831	0.03353	1.238

**Fig. 7** **a** Saturation magnetization and coercive field as function of Mn doped and **b** comparison between the experimental magnetic moment per unit formula and that estimated from the proposed cation distribution for Li_{0.5}Fe_{2.5-x}Mn_xO₄ nanoparticles

ferrite matrix increased. A similar effect was observed in Mn-doped NaMgGdTeO₆ [40] and Zn₂SiO₄ nanowires [41]. The reduction in the intensity of emission band can be correlated to the number of oxygen vacancies and interstitial metal defects generated in tetrahedral and octahedral sites of the investigated compositions [42]. The lower PL emission intensity reveals the decrease in recombination rate

**Fig. 8** PL spectra at excitation at 220 nm for Li_{0.5}Fe_{2.5-x}Mn_xO₄ nanoparticles

of photoinduced electron–hole pairs, which may be recognized to the form of new electronic levels between the conduction and the valence band and might be due to the increase in intrinsic defects [42]. Moreover, the PL spectra are blue-shifted for Li_{0.5}Fe_{1.5}MnO₈ sample with respect to all samples, due to a reduction of the crystallite size which confirmed the result obtained from X-ray diffraction investigation, Table 1. Furthermore, the PL spectra of all samples exhibited two UV sub-emissions and one green emission. The UV emissions may be due to near band-edge recombination [43]. While the green emission is linked to defects deeply placed in the band gap and to a greater disorder in the lattice or interstitial oxygen defects raised by distorted octahedral lattice [44].

4 Conclusions

Nano Mn-doped LiFe₅O₈ (Li_{0.5}Fe_{2.5-x}Mn_xO₄) was prepared with different Mn concentrations (0.0, 0.25, 0.50, 0.75 and 1.0) by citrate method at 400 °C. Bare LiFe₅O₈ is cubic ordered phase (P4₃32) and doping with Mn caused the transformation to the disordered phase (Fd $\bar{3}$ m), where percentage of disorder and ordered phases are greater than 92% and less than 8%, respectively, for all doped samples. The lattice parameter (a) and the z -coordinate (u) for oxygen atom remain almost constant, unaffected by Mn substitution. Infrared spectroscopy confirmed the presence of ordered phase for bare sample and two phases (ordered and disordered) for doped ones. The saturation magnetization and magneto anisotropy constant decreased generally with increasing Mn-doped amount. The PL spectra for Mn-doped samples are blue-shifted with regard to other samples, due

to a reduction of the crystallite size. Also, the PL spectra of all samples exhibited two UV sub-emissions and one green emission due to near band-edge recombination and defects inside the samples.

Acknowledgements Authors are grateful especially to Prof. H. Fuess from Technische Universität Darmstadt for neutron diffraction data.

References

- H. Zeng, T. Tao, Y. Wu, W. Qi, C. Kuang, S. Zhou, Y. Chen, RSC Adv **4**, 23145 (2014)
- S.J. Stewart, S.H. Al-Harhi, S. Thomas, H. Sitepu, J. Phys. D Appl. Phys. **41**, 165006 (2008)
- K.K. Kefeni, T.A. M.Msagati, B.B. Mamba, Mater. Sci. Eng. B **215**, 37 (2017)
- H. Zeng, T. Tao, Y. Wu, W. Qi, C.J. Kuang, S.X. Zhou, Y. Chen, RSC Adv. **4**, 23145 (2014)
- H.M. Widatallah, C. Johnson, A.M. Gismelseed, I.A. Al-Omari, S.J. Stewart, S.H. Al-Harhi, S. Thomas, H. Sitepu. J. Phys. D **41**, 165006 (2008)
- P. Naderi, S.M. Masoudpanah, S. Alamolhoda, Appl. Phys. A **123**, 702 (2017)
- S. Soreto, M. Graça, M. Valente, L. Costa, in *Magnetic Spinel—Synthesis, Properties and Applications*, ed. by M.S. Seehra (InTech, Rijeka, 2017)
- E. Kato, Bull. Chem. Soc. Jpn **31**, 113 (1958)
- K. El-Sayed, M.B. Mohamed, S. Hamdy, S.S. Ata-Allah, J. Magn. Magn. Mater. **423**, 291 (2017)
- N.G. Jović, A.S. Masadeh, A.S. Kremenović, B.V. Antić, J.L. Blanuša, N.D. Cvjetičanin, G.F. Goya, M.V. Antisari, E.S. Božin, J. Phys. Chem. C **113**(48), 20559 (2009)
- Y.P. Fu, C.S. Hsu, Solid State Commun. **134**, 201 (2005)
- B.K. Chougule, J. Magn. Magn. Mater **321**, 3270 (2009)
- H.M. Widatallah, F.N. Al-Mabsali, F.S. Al-HajriN., A.D. Al-Rawas, M. Elzain, A. Yousif, O. Khalifa, A.M. Gismelseed. Hyperfine Interact **237**, 50 (2016)
- J.S. Kounsalye, P.B. Kharat, D.N. Bhojar, K.M. Jadhav, J. Mater. Sci. Mater. Electron. **29**, 8601 (2018)
- P. Sharma, P. Thakur, J.L. Mattei, P. Queffelec, A. Thakur, J. Magn. Magn. Mater **407**, 17 (2016)
- L. Lutterotti, Nucl. Inst. Methods Phys. Res. B. **268**, 334 (2010)
- J. Rodríguez-Carvajal, Phys. B (Amsterdam, Neth.) **192**, 55 (1993)
- M.B. Mohamed, A. Senyshyn, H. Ehrenberg, H. Fuess, J. Alloys Compd. **492**(1–2), L20 (2010)
- E. Wolska, P. Piszora, J. Daeul, W. Nowicki, Mater. Sci. Forum **378**, 551 (2001)
- J. Darul, W. Nowicki, P. Piszora, C. Baetz, E. Wolska, J. Alloys Compd. **401**, 60 (2005)
- C. Wende, Kh Olimov, H. Modro, F.E. Wagner, H. Langbein, Mater. Res. Bull. **41**, 1530 (2006)
- J. Rodríguez-Carvajal, *Applied crystallography* (World Scientific, Singapore, 2001), pp. 30–36
- D. Alonso-Domínguez, I. Álvarez-Serrano, M.L. López, M.L. Veiga, C. Pico, F. Mompeán, M. García-Hernández, G.J. Cuello, J. Alloys Compd. **577**, 269 (2013)
- W.B. White, B.A. DeAngelis, Spectrochim Acta **23A**, 985 (1967)
- V.A.M. Brabers, Spectrochim Acta **32A**, 1709 (1976)
- V.A. Potakova, N.D. Zverv, V.P. Romanov, Phys. Stat. Sol. (A) **12**, 623 (1972)
- E. Wolska, P. Piszora, W. Nowicki, J. Darul, Inter. J. Inor. Mater. **3**, 503 (2001)
- F. Petit, M. Lenglet, Solid State Commun. **86**(2), 67 (1993)
- S.G. Gawas, S.S. Meena, S.M. Yusuf, V.M.S. Verenkar, New J. Chem. **40**, 9275 (2016)
- B.D. Cullity, C.D. Graham, *Introduction to Magnetic Materials (Google eBook)* (Wiley, Hoboken, 2011)
- M.M.L. Sonia, S. Anand, V.M. Vinosel, M.A. Janifer, S. Pauline, A. Manikandan, J. Magn. Magn. Mater. **466**, 238 (2018)
- B. Ramesh, M.L. Rao, J. Alloys Compd. **551**, 527–530 (2013)
- Z.K. Heiba, M.B. Mohamed, A.M. Wahba, L. Arda, J. Supercond. Nov. Magn **28**(8), 2517 (2015)
- T.R. M.Guire, F.S. Ferebee, J. Appl. Phys. **34**, 6 (1963)
- Z.K. Heiba, A. Abo-Shama, M. Bakr, K. El-Sayed, Powder Diffr. **22**(3), 256 (2007)
- L. Kumar, P. Kumar, M. Kar, Appl Nanosci **3**, 75 (2013)
- B.D. Cullity, *Introduction to Magnetic Materials* (Wiley, New Jersey, 2009)
- J.B. Goodenough, A.L. Loeb, Phys Rev **98**, 391 (1955)
- Y. Melikhov, J.E. Snyder, D.C. Jiles, A.P. Ring, J.A. Paulsen, C.C.H. Lo, K.W. Dennis, J. Appl. Phys. **99**, 08R102 (2006)
- K. Li, H. Lian, R.V. Deun, J. Lumin. **198**, 155 (2018)
- A.C. Roy, D. Mohanta, Philos Mag Lett **91**(6), 423 (2011)
- K. Fujihara, S. Izumi, T. Ohno, M. Matsumura, J. Photochem. Photobiol. A **132**, 99 (2000)
- Z.K. Heiba, M.B. Mohamed, N.G. Imam, J. Supercond. Nov. Magn **30**(11), 3123 (2017)
- J.J. Manikandan, L.J. Vijaya, M. Kennedy, Bououdina, J. Mol. Struct. **1035**, 332 (2013)